A Moving IRBFN-based Galerkin meshless method

Phong B.H. Le[1], Timon Rabczuk[2] Nam Mai-Duy[1] and Thanh Tran-Cong[1]

Abstract: A novel meshless method based on Radial Basis Function networks (RBFN) and variational principle (global weak form) is presented in this paper. In this method, the global integrated RBFN is localized and coupled with the moving least square method via the partition of unity concept. As a result, the system matrix is symmetric, sparse and banded. The trial and test functions satisfy the Kronecker-delta property, i.e. $\Phi_i(\mathbf{x}_j) = \delta_{ij}$. Therefore, the essential boundary conditions are imposed in strong form as in the FEMs. Moreover, the proposed method is applicable to scattered nodes and arbitrary domains. The method is examined with several numerical examples and the results indicate that the accuracy and the rate of convergence of the proposed method are superior to those of the EFG method using linear basis functions. In addition, the method does not exhibit any volumetric locking near the limit of incompressible material.

Keywords: RBF, Local IRBF, Moving IRBF, partition of unity, meshless, elasticity, crack, superconvergence.

1 Introduction

In recent years meshless methods have achieved remarkable progress. Works reported include [Belytschko, Lu, and Gu (1994); Li, Shen, Han, and Atluri (2003); Han and Atluri (2003); Atluri, Liu, and Han (2006); Mai-Duy, Khennane, and Tran-Cong (2007); Zhang and Chen (2008); Zheng, Wu, Tang, and Zhang (2008)]. Among meshless methods, the Element Free Galerkin (EFG) method introduced by Belytschko, Lu, and Gu (1994) has attracted much attention and been successfully applied to various engineering computations owing to its flexibility in solving problems with moving boundaries and moving discontinuities such as evolving crack and shear band formation.

In comparison with FEM, the EFG meshless method enjoys a number of advantages. For example, the latter does not require a mesh for the interpolation process; offers a higher order of continuity;

[1] CESRC, University of Southern Queensland, Toowoomba, QLD 4350, Australia.
[2] Institute of Structural Mechanics, Bauhaus-University Weimar, Marienstr. 15, 99423 Weimar, Germany.

and may not suffer so much degradation in accuracy as nodal arrangements are irregular. Moreover, EFG is more suitable for adaptivity and able to alleviate the effects of volumetric locking at the limit of incompressible materials provided that the local support radius is large enough. However, the major disadvantage of EFG as well as Moving Least Square (MLS) based meshless methods is that the shape functions lack the Kronnecker-delta property, i.e. $\Phi_i(\mathbf{x}_j) \neq \delta_{ij}$. The essential boundary conditions are not easy to be imposed accurately as in the FEMs due to this inequality. Attempts to overcome this shortcoming include Lagrange multiplier and penalty method [Zhu and Atluri (1998)], Nitsche's method [Fernández-Mández and Huerta (2004)], point collocation [Wanger and Liu (1999)], singular weight functions [Kaljevic and Saigal (1997)], coupling with FEM [Belytschko, Organ, and Krongauz (1995)]. Another alternative approach to address this limitation is employing the interpolation techniques that possess the Kronecker-delta property in constructing the shape functions of meshless Galerkin method. Examples include point interpolation meshless method [Wang and Liu (2002)], radial point interpolation method [Liu, Zhang, and Gu (2005)], and moving Kriging method [Gu (2003)].

Motivated by the former works, this paper proposes a novel meshless method based on (i) Moving Integrated Radial Basis Function Network (MIRBFN) and (ii) (global weak form) Galerkin formulation, resulting in Moving IRBFN Galerkin (MIRBFNG) meshless method. In the present method, the shape functions are constructed within subdomains instead of the global domain. The system matrix is thus sparse and banded. The shape functions satisfy the Kronnecker-delta property, therefore, essential boundary conditions are imposed easily and straightforwardly as in the FEMs. Moreover, the proposed method is applicable to irregular distributions of nodes and arbitrary domains. The remaining of this work is organized as follows. The MIRBFN is briefly presented in section 2 followed by the Galerkin formulation for elasticity problems in section 3. Section 4 reports the numerical experiments and section 5 draws some conclusions.

2 MOVING IRBFN PROCEDURE

2.1 The global IRBFN approximation

In the IRBFN method [Mai-Duy and Tran-Cong (2001, 2005); Mai-Duy and Tanner (2005); Le, Mai-Duy, Tran-Cong, and Baker (2007, 2008)], the highest order derivatives of a function u, e.g. $\frac{\partial^2}{\partial x_j^2}u(\mathbf{x})$, are represented by RBFNs. The derivative expressions obtained are then integrated to

yield expressions for lower order derivatives and finally for the original function as follows.

$$\frac{\partial^2}{\partial x_j^2}u(\mathbf{x}) = \sum_{i=1}^{m} w^{(i)} g^{(i)}(\mathbf{x}), \tag{1}$$

$$\frac{\partial}{\partial x_j}u(\mathbf{x}) = \int \sum_{i=1}^{m} w^{(i)} g^{(i)}(\mathbf{x}) dx_j + C_1(x_{l;l\neq j}) = \sum_{i=1}^{m+p_1} w^{(i)} H_{[x_j]}^{[1](i)}(\mathbf{x}), \tag{2}$$

$$u(\mathbf{x}) = \int \sum_{i=1}^{m+p_1} w^{(i)} H_{[x_j]}^{[1](i)}(\mathbf{x}) dx_j + C_2(x_{l;l\neq j}) = \sum_{i=1}^{m+p_2} w^{(i)} H_{[x_j]}^{[0](i)}(\mathbf{x}), \tag{3}$$

where, the subscripts $[x_j]$ denote variables associated with partial differentiation, m is the number of RBF centers, $\{g^{(i)}(\mathbf{x})\}_{i=1}^{m}$ the set of RBFs, $\{C_i\}_{i=1}^{2}$ the set of constants arising from integration, $\{w^{(i)}\}_{i=1}^{m+p_2}$ the set of corresponding network weights to be found, $\{H_{[x_j]}^{[1](i)}(\mathbf{x})\}_{i=1}^{m}$, $\{H_{[x_j]}^{[0](i)}(\mathbf{x})\}_{i=1}^{m}$ the newly derived basis functions relating to the first derivative and the original function $u(\mathbf{x})$, respectively, p_1, p_2 the number of centers used to represent integration constants ($p_2 = 2p_1$).

Collocating (1)-(3) at the set of L nodal points $\{\mathbf{x}^{(c)}\}_{c=1}^{L}$ leads to

$$\mathbf{u}_{,jj} = \mathbf{G}\mathbf{w}_{[x_j]}, \tag{4}$$

$$\mathbf{u}_{,j} = \mathbf{H}_{[x_j]}^{[1]}\mathbf{w}_{[x_j]}, \tag{5}$$

$$\mathbf{u} = \mathbf{H}_{[x_j]}^{[0]}\mathbf{w}_{[x_j]}, \tag{6}$$

where $\mathbf{u}$ is the vector of nodal values of u, $\mathbf{G}$ the matrix whose p^{th} row is comprised of $\{g^{(i)}(\mathbf{x}^{(p)})\}_{i=1}^{m}$ and $\{0\}_{i=1}^{p_2}$, and $\mathbf{H}_{[x_j]}^{[l]}$ the matrix whose p^{th} row is comprised of $\{H_{[x_j]}^{[l](i)}(\mathbf{x}^{(p)})\}_{i=1}^{m+p_l}$ and $\{0\}_{i=1}^{p_2-p_l}$. For the multiquadric function

$$g^{(i)}(\mathbf{x}) = \sqrt{\left\|\mathbf{x} - \mathbf{c}^{(i)}\right\|^2 + \left(a^{(i)}\right)^2}, \tag{7}$$

where $\mathbf{c}^{(i)}$ is the RBF center and $a^{(i)}$ the RBF width, the width of the i^{th} RBF can be determined according to the following simple relation

$$a^{(i)} = \beta d^{(i)}, \tag{8}$$

where β is a factor, $\beta > 0$, and $d^{(i)}$ is the distance from the i^{th} center to its nearest center.

We perform a prior conversion of the unknowns from network weights, e.g., $\{w^{(i)}\}_{i=1}^{m+p_2}$, into nodal

function value $\mathbf{u}$ in order to form a square system of equations of smaller size as follows. The network weights are expressed in terms of nodal function values as

$$\mathbf{w}_{[x_j]} = \left[\mathbf{H}^{[0]}_{[x_j]}\right]^{-1}\mathbf{u}. \tag{9}$$

Substitution of (9) into the system (4)-(6) yields

$$\mathbf{u}_{,jj} = \mathbf{G}\left[\mathbf{H}^{[0]}_{[x_j]}\right]^{-1}\mathbf{u}, \tag{10}$$

$$\mathbf{u}_{,j} = \mathbf{H}^{[1]}_{[x_j]}\left[\mathbf{H}^{[0]}_{[x_j]}\right]^{-1}\mathbf{u}, \tag{11}$$

$$\mathbf{u} = \mathbf{H}^{[0]}_{[x_j]}\left[\mathbf{H}^{[0]}_{[x_j]}\right]^{-1}\mathbf{u} = \mathbf{I}\mathbf{u}, \tag{12}$$

where $\mathbf{I}$ is the identity matrix.

2.2 Moving least-square approximants

The moving least-square (MLS) method was originally developed by Lancaster (1981) for curve-fitting problem and later on applied in the context of the element-free Galerkin method [Belytschko, Lu, and Gu (1994)]. The principal property of MLS is to exactly reproduce a given set of functions. Therefore, an approximation $u^h(\mathbf{x})$ of the function $u(\mathbf{x}) \in \Omega$ is given by

$$u^h(\mathbf{x}) = \sum_{I=1}^{M} a_I(\mathbf{x})p_I(\mathbf{x}) \tag{13}$$

where $\mathbf{p}$ is the basis vector containing M functions that need to be reproduced, $\mathbf{x}^T = [x,y]$, and $a_I(\mathbf{x})$ are unknown coefficients depending on $\mathbf{x}$. In this paper, we use a linear basis, i.e. $\mathbf{p}^T = [1,x,y]$.

The unknown coefficients $a_I(\mathbf{x})$ in (13) are obtained by minimizing the quadratic form

$$\mathscr{J} = \sum_{J=1}^{n} w(\mathbf{x}-\mathbf{x}_J)\left(\mathbf{p}^T(\mathbf{x}_J)\mathbf{a}(\mathbf{x}) - u_J\right)^2, \tag{14}$$

where n is the number of points in the neighbourhood of $\mathbf{x}$ for which the weight function $w(\mathbf{x}-\mathbf{x}_J) \neq 0$, and u_J is the nodal value of u at $\mathbf{x} = \mathbf{x}_J$.

Minimizing the discrete weighted L_2 norm $\mathscr{J}$ in (14) with respect to $\mathbf{a}(\mathbf{x})$ leads to a linear relation between $\mathbf{a}(\mathbf{x})$ and u_I, that can be solved for $\mathbf{a}(\mathbf{x})$ which is then substituted into (13) to obtain the

final MLS approximation

$$u^h(\mathbf{x}) = \sum_{I=1}^{n} \varphi_I(\mathbf{x}) u_I, \tag{15}$$

with MLS shape functions

$$\varphi_I(\mathbf{x}) = \sum_{J=1}^{M} \sum_{K=1}^{n} p_J(\mathbf{x}) A^{-1}_{JK}(\mathbf{x})\ B_{KI}(\mathbf{x}) \tag{16}$$

and

$$\begin{aligned} \mathbf{A}(\mathbf{x}) &= \sum_{I=1}^{n} w(\mathbf{x}-\mathbf{x}_I)\mathbf{p}(\mathbf{x}_I)\mathbf{p}^T(\mathbf{x}_I), \\ \mathbf{B}_{(:,I)}(\mathbf{x}) &= w(\mathbf{x}-\mathbf{x}_I)\mathbf{p}(\mathbf{x}_I), \end{aligned} \tag{17}$$

where the subscript $(:,I)$ denotes column I of $\mathbf{B}$.

In this paper, we use the quartic spline kernel function

$$w(r) = \begin{cases} 1-6\left(\frac{r}{R_s}\right)^2+8\left(\frac{r}{R_s}\right)^3-3\left(\frac{r}{R_s}\right)^4, & \frac{r}{R_s} \le 1; \\ 0, & \frac{r}{R_s} > 1, \end{cases} \tag{18}$$

where $r = \|\mathbf{x}-\mathbf{x}_I\|$, $\|.\|$ denotes the Euclidean norm, and R_s is the radius of the support domain of the weight function $w(r)$ defined by

$$R_s = \alpha h, \tag{19}$$

in which h is a characteristic length that relates to the nodal spacing around the point of interest and α is a scale factor.

2.3 Moving IRBFN interpolation

The moving IRBFN method using partition of unity concept [Melenk and Babuška (1996); Babuška and Melenk (1997)] is as follows.

Let the open and bounded domain of interest $\Omega \subseteq \mathbb{R}^d$ be discretised by a set of N points $\mathscr{X}$

$$\mathscr{X} = \{\mathbf{x}_1, \mathbf{x}_2, \ldots, \mathbf{x}_N\}, \qquad \mathbf{x}_I \in \Omega, \qquad I = 1,2,\ldots,N, \tag{20}$$

$\mathscr{X}$ is used to define a set of finite open cover of Ω, i.e., $\{\Omega_I\}$ such that $\Omega \subseteq \bigcup_{I=1}^{N} \Omega_I$ and $\{\Omega_I\}$ satisfies a point-wise overlap condition

$$\forall \mathbf{x} \in \Omega \qquad \exists k \in \mathbb{N} \qquad : \qquad \text{card}\{I | \mathbf{x} \in \Omega_I\} \leq k. \tag{21}$$

We choose a family of compactly supported, non-negative, continuous functions ψ_I supported on the closure of Ω_I, such that at every point $\mathbf{x}$ we have the following property

$$\sum_{I=1}^{N} \psi_I(\mathbf{x}) = 1, \qquad \forall \mathbf{x} \in \Omega, \tag{22}$$

where $\{\psi_I\}$ is called a partition of unity subordinate to the cover $\{\Omega_I\}$.
For every subdomain Ω_I, a local approximation u_I is constructed by using global IRBFN presented in section 2.1, i.e.,

$$u_I^h(\mathbf{x}) \in V_I, \qquad V_I = \text{span}\{V_I^1, V_I^2, ..., V_I^L\}, \tag{23}$$

where $\{V_I\}$ are referred to as the local approximation spaces and V_I^k is the k-th element of the vector defined by

$$\left[H_{[x_j]I}^{[0](1)}(\mathbf{x}), H_{[x_j]I}^{[0](2)}(\mathbf{x}), \ldots, H_{[x_j]I}^{[0](m+p_k)}(\mathbf{x})\right] \left[\mathbf{H}_{[x_j]}^{[0]}\right]^{-1}.$$

The global approximation of $u(\mathbf{x})$, $u^h(\mathbf{x})$, is obtained via

$$u^h(\mathbf{x}) = \sum_{I=1}^{N} \psi_I(\mathbf{x}) u_I^h(\mathbf{x}), \qquad u^h(\mathbf{x}) \in V, \tag{24}$$

where $\psi_I(\mathbf{x})$ and $u_I^h(\mathbf{x})$ are associated with the subdomain Ω_I, and V is called PUM space and defined by

$$V := \sum_{I=1}^{N} \psi_I V_I. \tag{25}$$

In the present work, the partition of unity function ψ_I is chosen to be the MLS shape function φ_I in (16), the subdomain Ω_I is centered at $\mathbf{x}_I$ as shown in Figure 1.

Replacing ψ_I with MLS shape function φ_I, (24) can be rewritten as follows

$$u^h(\mathbf{x}) = \sum_{I=1}^{N} \varphi_I(\mathbf{x}) u_I^h(\mathbf{x}), \tag{26}$$

and the associated derivatives of $u^h(\mathbf{x})$ are

$$u^h_{,x}(\mathbf{x}) = \sum_{I=1}^{N} \left[\varphi_{I,x}(\mathbf{x}) u_I^h(\mathbf{x}) + \varphi_I(\mathbf{x}) u^h_{I,x}(\mathbf{x}) \right], \tag{27}$$

$$u^h_{,y}(\mathbf{x}) = \sum_{I=1}^{N} \left[\varphi_{I,y}(\mathbf{x}) u_I^h(\mathbf{x}) + \varphi_I(\mathbf{x}) u^h_{I,y}(\mathbf{x}) \right], \tag{28}$$

where $u^h_{,x}(\mathbf{x})$, $u^h_{,y}(\mathbf{x})$, are derived in (11).
$u^h(\mathbf{x})$ and its derivatives can be expressed in a compact form as

$$u^h(\mathbf{x}) = \mathbf{\Phi}^T(\mathbf{x})\mathbf{u}, \tag{29}$$

$$u^h_{,x}(\mathbf{x}) = \mathbf{\Phi}^T_{,x}(\mathbf{x})\mathbf{u}, \tag{30}$$

$$u^h_{,y}(\mathbf{x}) = \mathbf{\Phi}^T_{,y}(\mathbf{x})\mathbf{u}, \tag{31}$$

where $\mathbf{u} = \{u_1, u_2, \ldots, u_N\}$, $\mathbf{\Phi}(\mathbf{x})$ is the vector of shape functions, $\mathbf{\Phi}_{,x}(\mathbf{x})$ and $\mathbf{\Phi}_{,y}(\mathbf{x})$ can be determined by substitution of (11) into equations (27) and (28), respectively, as follows.

$$\begin{aligned}\mathbf{\Phi}_{,x}(\mathbf{x}) =& \varphi_{,x}(\mathbf{x}) \left[H^{[0](1)}_{[x]}(\mathbf{x}), H^{[0](2)}_{[x]}(\mathbf{x}), \ldots, H^{[0](m+p_k)}_{[x]}(\mathbf{x}) \right] \left[\mathbf{H}^{[0]}_{[x]} \right]^{-1} + \\ & \varphi(\mathbf{x}) \left[H^{[1](1)}_{[x]}(\mathbf{x}), H^{[1](2)}_{[x]}(\mathbf{x}), \ldots, H^{[1](m+p_k)}_{[x]}(\mathbf{x}) \right] \left[\mathbf{H}^{[0]}_{[x]} \right]^{-1}, \end{aligned} \tag{32}$$

$$\begin{aligned}\mathbf{\Phi}_{,y}(\mathbf{x}) =& \varphi_{,y}(\mathbf{x}) \left[H^{[0](1)}_{[y]}(\mathbf{x}), H^{[0](2)}_{[y]}(\mathbf{x}), \ldots, H^{[0](m+p_k)}_{[y]}(\mathbf{x}) \right] \left[\mathbf{H}^{[0]}_{[y]} \right]^{-1} + \\ & \varphi(\mathbf{x}) \left[H^{[1](1)}_{[y]}(\mathbf{x}), H^{[1](2)}_{[y]}(\mathbf{x}), \ldots, H^{[1](m+p_k)}_{[y]}(\mathbf{x}) \right] \left[\mathbf{H}^{[0]}_{[y]} \right]^{-1}. \end{aligned} \tag{33}$$

It is noted that $\Phi_I(\mathbf{x}_J) = \delta_{IJ}$ as shown in Figures 2 and 3. Consequently, the present MIRBFN method possesses the Kronecker-delta property which makes it easy and efficient to impose the essential boundary conditions.

3 Variational form of two dimensional elasticity problems

Consider the following two-dimensional problem on a domain Ω bounded by $\Gamma = \Gamma_u \bigcup \Gamma_t$

$$\nabla \cdot \sigma + \mathbf{b} = 0 \qquad \text{in} \quad \Omega, \tag{34a}$$

$$\mathbf{u} = \bar{\mathbf{u}} \qquad \text{on} \quad \Gamma_u, \tag{34b}$$

$$\sigma \cdot \mathbf{n} = \bar{\mathbf{t}} \qquad \text{on} \quad \Gamma_t, \tag{34c}$$

where σ is the stress tensor, which corresponds to the displacement field $\mathbf{u}$ and $\mathbf{b}$ the body force, $\mathbf{n}$ the outward unit normal to Γ_t. The superimposed bar denotes prescribed value on the boundary. The weak form for the above equations is expressed as

$$\int_\Omega \delta(\nabla_s \mathbf{u})^T \sigma d\Omega = \int_\Omega \delta \mathbf{u}^T \mathbf{b} d\Omega + \int_{\Gamma_t} \delta \mathbf{u}^T \bar{\mathbf{t}} d\Gamma, \tag{35}$$

where the subscript s denotes the symmetric part of the gradient operator. Discretization of (35) with Moving IRBFNs yields

$$\mathbf{K}\mathbf{u} = \mathbf{f}, \tag{36}$$

where

$$\mathbf{K}^{ij} = \int_\Omega \mathbf{B}^{iT} \mathbf{C} \mathbf{B}^j d\Omega, \tag{37}$$

are 2×2 matrices to be assembled into the global matrix $\mathbf{K}$ at positions associated with nodes i and j as in a FEM procedure,

$$\mathbf{f}^i = \int_{\Gamma_t} \Phi^i \bar{\mathbf{t}} d\Gamma + \int_\Omega \Phi^i \mathbf{b} d\Omega, \tag{38}$$

are 2×1 vectors to be assembled into the global vector $\mathbf{f}$ at positions associated with node i as in

a FEM procedure,

$$\mathbf{B}^i = \begin{bmatrix} \Phi^i_{,x} & 0 \\ 0 & \Phi^i_{,y} \\ \Phi^i_{,y} & \Phi^i_{,x} \end{bmatrix}. \tag{39}$$

For the linear Hookean constitutive relation, the matrix $\mathbf{C}$ in the case of plane stress is

$$\mathbf{C} = \frac{E}{1-\nu^2} \begin{pmatrix} 1 & \nu & 0 \\ \nu & 1 & 0 \\ 0 & 0 & \frac{1-\nu}{2} \end{pmatrix}, \tag{40}$$

where E is the elastic modulus and ν the Poisson's ratio.

In global weak form discretisation, a background mesh independent of data nodes is necessary for numerical integration of (37)-(38), and Gauss quadrature is employed for the numerical integration in this work. A noteworthy feature of the present method is that the essential boundary condition is imposed easily and straightforwardly as in the FEM.

4 Numerical examples

For error estimation and convergence study, the displacement norm and energy norm are defined as follows.

$$\text{displacement norm} = \sqrt{\int_\Omega (\mathbf{u}^{num} - \mathbf{u}^{exact})^T (\mathbf{u}^{num} - \mathbf{u}^{exact}) d\Omega}, \tag{41}$$

$$\text{energy norm} = \sqrt{\frac{1}{2}\int_\Omega (\varepsilon^{num} - \varepsilon^{exact})^T (\sigma^{num} - \sigma^{exact}) d\Omega}, \tag{42}$$

where the superscripts *num* and *exact* denote numerical and exact solutions, respectively; the stress and strain components are presented in vector form as σ and ε, respectively.

The convergence order of the solution with respect to the refinement of spatial discretization is

assumed to be in the form of

$$error(h) \approx \zeta h^{\lambda} = O(h^{\lambda}), \tag{43}$$

where h is the maximum nodal spacing, ζ and λ are the parameters of the exponential model, which are found by general linear least square formula.

It is noted that the present results are compared with those obtained by the EFG method which only uses linear basis function.

4.1 One dimensional example

Consider a one-dimensional bar of unit length ($L = 1$) subjected to a linear body force of magnitude x as shown in Figure 4. The bar is fixed at the left end and traction free at the right end. The cross sectional area of the bar is of unit value and the modulus of elasticity is $E = 1$.

The equilibrium equation and boundary conditions for this problems are as follows.

$$E\frac{\partial^2 u}{\partial x^2} + x = 0, \qquad 0 \le x \le 1 \tag{44}$$

$$u(0) = 0, \tag{45}$$

$$\frac{\partial u}{\partial x}(1) = 0. \tag{46}$$

The exact solution to the problem is given by

$$u(x) = \frac{1}{E}\left[\frac{1}{2}x - \frac{x^3}{6L^2}\right]. \tag{47}$$

In this example, the domain is uniformly discretised, α and β are set at 2.1 and 4, respectively. Seven Gauss points are employed in each cell (defined by two adjacent nodes) for the numerical integration.

Figure 5 shows the numerical solution obtained by the present method with uniform distribution of 9 nodes and the results are interpolated at 50 points. It can be seen that the numerical solution excellently agrees with the exact solution. Moreover, the accuracy of the present method is favourably compared with that of the EFG method as shown in Figures 5-6.

The rates of convergence of the present method, using displacement and energy norms are 2.73

and 1.87, respectively, while those of the EFG method are 2.50 and 1.48, respectively, as displayed in Figures 7-8.

4.2 Cantilever Beam

The present method is now verified, using the problem of a cantilever beam subject to parabolic shear load at the end $x = 0$ as shown in Figure 9. The following parameters are used for the problem: $L = 4.8$ and $D = 1.2$. The beam has a unit thickness. Young's modulus is $E = 3 \times 10^6$, Poisson's ratio is $\mu = 0.3$ (also $\mu = 0.4999$) and the integrated parabolic shear force is $P = 100$. Plane stress condition is assumed and there is no body force.

The exact solution to this problem was given by Timoshenko and Goodier (1970) as

$$\sigma_{xx}(x,y) = \frac{-Pxy}{I}, \tag{48a}$$

$$\sigma_{yy}(x,y) = 0, \tag{48b}$$

$$\tau_{xy}(x,y) = \frac{-P}{2I}\left(\frac{D^2}{4} - y^2\right). \tag{48c}$$

The displacements are given by

$$u_x = -\frac{Px^2y}{2EI} - \frac{\mu Py^3}{6EI} + \frac{Py^3}{6IG} + y\left(\frac{PL^2}{2EI} - \frac{PD^2}{8IG}\right), \tag{49}$$

$$u_y = \frac{\mu Pxy^2}{2EI} + \frac{Px^3}{6EI} - \frac{PL^2x}{2EI} + \frac{PL^3}{3EI}, \tag{50}$$

where $I = D^3/12$ is the moment of inertia of the cross section of the beam (of unit thickness), $G = E/(2(1+\mu))$ the modulus of elasticity in shear.

The exact displacements (49) and (50) are applied on the Dirichlet boundary $x = L$.

To solve this problem, uniform distributions of nodes (Figure 10) are considered. The scale factor of local support α is set at 2.1 and β is 9. Background meshes of four-node cells with 4×4 Gauss quadrature points per cell are used for the numerical integration.

Figure 11 illustrates the comparison between the stress (σ_x) obtained by the proposed method with 20×5 nodes and the exact one. Figures 12 and 13 show the convergence behaviour of the method using displacement and energy norms, respectively. High orders of convergence achieved by the present method can be observed in the figures, i.e. $O(h^{5.21})$ and $O(h^{2.95})$ ($\mu = 0.3$) using displace-

ment and energy norms, respectively. The stress plots (Figure 11) together with the error norms (Figures 12-13) show an excellent agreement between the numerical results and the analytical solution. Furthermore, the numerical results in the case of $\mu = 0.4999$ indicate that the MIRBFNG method does not suffer from any volumetric locking near the limit of incompressible material.

For the purpose of comparison, the same configurations of nodes, local supports and background meshes are used for the EFG method with 4×4 Gauss quadrature points in each integration cell. The comparison shows that the rates of convergence and the accuracy achieved by the present method are superior to those obtained by the EFG as shown in the above figures.

To study the performance of the method with sets of scattered nodes ($\mu = 0.3$), the domain of interest is discretised with 125, 225, 633, 803, 1020, 1725 and 2502 unstructured nodes as depicted in Figure 14. The convergence of τ_{xy} at $x = 2.40$ is revealed in Figure 15. It can be observed that the method performs very well with scattered distribution of nodes. The convergence rates using displacement and energy norms obtained by the present method are 3.95 and 1.72, respectively (Figures 16-17).

4.3 Infinite plate with a circular hole

In this example, an infinite plate with a circular hole subjected to unidirectional tensile load of 1.0 in the x direction as shown in Figure 18 is analyzed. The radius of the hole is taken as 1 unit. Owing to symmetry, only the upper right quadrant $[0,4] \times [0,4]$ of the plate is modeled as shown in Figure 19.

In this problem, plane stress conditions are assumed with elastic isotropic properties $E = 10^3$, $\mu = 0.3$. The exact solution to this problem was given by Timoshenko and Goodier (1970) as follows.

$$\sigma_x(x,y) = \sigma \left[1 - \frac{a^2}{r^2} \left[\frac{3}{2}\cos(2\theta) + \cos(4\theta) \right] + \frac{3a^4}{2r^4}\cos(4\theta) \right], \tag{51a}$$

$$\sigma_y(x,y) = -\sigma \left[\frac{a^2}{r^2} \left[\frac{1}{2}\cos(2\theta) - \cos(4\theta) \right] + \frac{3a^4}{2r^4}\cos(4\theta) \right], \tag{51b}$$

$$\tau_{xy}(x,y) = -\sigma \left[\frac{a^2}{r^2} \left[\frac{1}{2}\sin(2\theta) + \sin(4\theta) \right] - \frac{3a^4}{2r^4}\sin(4\theta) \right], \tag{51c}$$

where (r,θ) are the polar coordinates, a the radius of the hole.

The corresponding displacements are given by

$$u_x(x,y) = \sigma\frac{(1+\mu)}{E}\left[\frac{1}{1+\mu}r\cos(\theta)+\frac{2}{1+\mu}\frac{a^2}{r}\cos(\theta)+\frac{1}{2}\frac{a^2}{r}\cos(3\theta)-\frac{1}{2}\frac{a^4}{r^3}\cos(3\theta)\right] \tag{52a}$$

$$u_y(x,y) = \sigma\frac{(1+\mu)}{E}\left[\frac{-\mu}{1+\mu}r\sin(\theta)+\frac{1-\mu}{1+\mu}\frac{a^2}{r}\sin(\theta)+\frac{1}{2}\frac{a^2}{r}\sin(3\theta)-\frac{1}{2}\frac{a^4}{r^3}\sin(3\theta)\right] \tag{52b}$$

The boundary conditions of the problem are as follows. The tractions which correspond to the exact solution for the infinite plate are applied on the top and right edges, the symmetric conditions are applied on the left and bottom edges, and the edge of the hole is traction free.

The computational domain ABCD is shown in Figure 22. Owing to symmetry, only the upper half of ABCD, namely CDEFG as shown in Figure 23, is analyzed. The segment of the crack denoted by EF has a length of $b = 5$ *mm*. The boundary condition of the problem is as follows. The traction free boundary condition is applied on the crack while the displacement field given in (54) is imposed on the remaining boundaries.

The problem is discretised as shown in Figure 19. The value of α and β are 1.5 and 1, respectively. The number of Gauss quadrature points per integration cell is 4×4.

To study the convergence of the method, a number of configurations of 50, 120, 315, 511 nodes is considered. Figures 20-21 show that the present method achieves excellent accuracy and high rates of convergence, i.e. 2.91 and 1.45 using displacement and energy norms, respectively. Again, it can be seen that the accuracy and the convergent rates of the proposed method are favourably compared with those of the EFG method as shown in the figures.

4.4 Mode I crack problem

Consider an infinite plate containing a straight crack of length $2a$ and loaded by a remote uniform stress field σ as shown in Figure 22. Under plane strain condition, the closed form solution in terms of polar coordinates in a reference frame (r,θ) centered at the crack tip is given by (body force is zero) [Tada, Paris, and Irwin (2000)]

$$\sigma_x = \frac{K_I}{\sqrt{r}}\cos\frac{\theta}{2}\left(1-\sin\frac{\theta}{2}\sin 3\frac{\theta}{2}\right), \tag{53a}$$

$$\sigma_y = \frac{K_I}{\sqrt{r}}\cos\frac{\theta}{2}\left(1+\sin\frac{\theta}{2}\sin 3\frac{\theta}{2}\right), \tag{53b}$$

$$\tau_y = \frac{K_I}{\sqrt{r}}\sin\frac{\theta}{2}\cos\frac{\theta}{2}\cos 3\frac{\theta}{2}, \tag{53c}$$

and the closed form of near tip displacement field is given by

$$u_x = \frac{2(1+\mu)}{\sqrt{2\pi}}\frac{K_I}{E}\sqrt{r}\cos\frac{\theta}{2}\left(2-2\mu-\cos^2\frac{\theta}{2}\right), \tag{54a}$$

$$u_y = \frac{2(1+\mu)}{\sqrt{2\pi}}\frac{K_I}{E}\sqrt{r}\sin\frac{\theta}{2}\left(2-2\mu-\cos^2\frac{\theta}{2}\right), \tag{54b}$$

where $K_I = \sigma\sqrt{\pi a}$ is the stress intensity factor, μ is the Poisson's ratio and E is the Young modulus. ABCD is a square of $10\times 10\ mm^2$, $a = 100\ mm$; $E = 10^7 N/mm^2$, $\mu = 0.3$ (also $\mu = 0.4999$), $\sigma = 10^4 N/mm^2$.

In this example, the domain of interest is uniformly discretised. α and β are 1.1 and 1, respectively. 2×2 Gauss quadrature points per integration cell are used for the numerical integration.

The numerical solutions to displacement and stress obtained with 20×10 nodes ($\mu = 0.3$) and the analytical solutions are plotted in Figures 24-26. The comparison indicates an excellent agreement between the solutions obtained by the proposed method and the exact solutions.

For convergence study, a number of regular distribution of 4×8, 8×16, 12×24, 16×32, 20×40, and 24×48 nodes is employed with $\mu = 0.3$ and $\mu = 0.4999$. The convergence curves for displacement and energy are shown in Figures 27 and 28, respectively. The orders of convergence using displacement and energy norms are 1.35 and 0.48, respectively, for $\mu = 0.3$. It can be seen that the rate of convergence for energy is reduced significantly due to singularity in the stress field. Again, the numerical results demonstrate that the method does not show any volumetric locking in the case of $\mu = 0.4999$ (Figures 27-28).

5 Concluding remarks

This work proposes a novel meshless method based on the MIRBFN interpolation and Galerkin method for solving PDEs. The key feature of the method is that the shape functions are locally supported and satisfy the Kronecher-delta property. As a result, the essential boundary conditions are imposed exactly and straightforwardly in this method. The method is applicable to sets of scattered nodes and irregular domains. Furthermore, the proposed method achieves high orders of convergence and high accuracy for smooth problems. The obtained results also indicate that there is no evidence of volumetric locking with the present method. Furthermore, it is encouraging that the accuracy and the rate of convergence of the method is favourably compared with those of the EFG method. As a result of coupling MLS technique with 'local' IRBFN method, the computational cost of the present Moving IRBFN approach is much better than that of the global IRBFN method but still higher than that of the MLS technique. The order of magnitude of the improvement in efficiency was reported in Le, Rabczuk, Mai-Duy, and Tran-Cong (2010).

Acknowledgement: This work is supported by the Australian Research Council. This support is gratefully acknowledged.

References

Atluri, S. N.; Liu, H. T.; Han, Z. D. (2006): Meshless local Petrov-Galerkin (MLPG) mixed collocation method for elasticity problems. *CMES: Computer Modeling in Engineering & Sciences*, vol. 14, no. 3, pp. 141–152.

Babuška, I.; Melenk, I. (1997): The partition of unity method. *International Journal for Numerical Methods in Engineering*, vol. 40, no. 4, pp. 727–758.

Belytschko, T.; Lu, Y. Y.; Gu, L. (1994): Element-free Galerkin methods. *International Journal for Numerical Methods in Engineering*, vol. 37, pp. 229–256.

Belytschko, T.; Organ, D.; Krongauz, Y. (1995): A couple finite element-element free Garlerkin method. *Computational Mechanics*, vol. 17, no. 3, pp. 186–195.

Fernández-Mández, S.; Huerta, A. (2004): Imposing essential boundary conditions in meshfree methods. *Computer Methods in Applied Mechanics and Engineering*, vol. 193, pp. 1257–1275.

Gu, L. (2003): Moving Kriging interpolation and element-free Galerkin method. *International Journal for Numerical Methods in Engineering*, vol. 56, pp. 1–11.

Han, Z. D.; Atluri, S. N. (2003): Truly meshless local petrov-galerkin (MLPG) solutions of traction & displacement BIEs. *CMES: Computer Modeling in Engineering & Sciences*, vol. 4, no. 6, pp. 665–678.

Kaljevic, J.; Saigal, S. (1997): An improved element free Galerkin formulation. *International Journal for Numerical Methods in Engineering*, vol. 40, pp. 2953–2974.

Lancaster, G. M. (1981): Surfaces generated by moving least squares methods. *Math. Comput.*, vol. 3, no. 37, pp. 141–158.

Le, P.; Mai-Duy, N.; Tran-Cong, T.; Baker, G. (2007): A numerical study of strain localization in elasto-therno-viscoplastic materials using radial basis function networks. *CMC: Computers, Materials & Continua*, vol. 5, pp. 129–150.

Le, P.; Mai-Duy, N.; Tran-Cong, T.; Baker, G. (2008): A meshless modeling of dynamic strain localization in quasi-britle materials using radial basis function networks. *CMES: Computer Modeling in Engineering & Sciences*, vol. 25, no. 1, pp. 43–66.

Le, P.; Rabczuk, T.; Mai-Duy, N.; Tran-Cong, T. (2010): A moving IRBFN-based integration-free meshless method. *CMES: Computer Modeling in Engineering & Sciences*, vol. 61, no. 1, pp. 63–109.

Li, Q.; Shen, S.; Han, Z. D.; Atluri, S. N. (2003): Application of meshless local Petrov-Galerkin (MLPG) to problems with singularities, and material discontinuities, in 3-D elasticity. *CMES: Computer Modeling in Engineering & Sciences*, vol. 4, no. 5, pp. 571–585.

Liu, G.; Zhang, G.; Gu, Y. (2005): A meshfree radial point interpolation method (RPIM) for three-dimensional solids. *Computational Mechanics*, vol. 36, no. 6, pp. 421–430.

Mai-Duy, N.; Khennane, A.; Tran-Cong, T. (2007): Computation of laminated composite plates using indirect radial basis function networks. *CMC: Computers, Materials & Continua*, vol. 5, pp. 63–77.

Mai-Duy, N.; Tanner, R. I. (2005): Solving high order partial differential equations with indirect radial basis function networks. *International Journal for Numerical Methods in Engineering*, vol. 63, pp. 1636–1654.

Mai-Duy, N.; Tran-Cong, T. (2001): Numerical solution of differential equations using multi-quadric radial basic function networks. *Neural Networks*, vol. 14, pp. 185–199.

Mai-Duy, N.; Tran-Cong, T. (2005): An efficient indirect RBFN-based method for numerical solution of PDEs. *Numerical Methods for Partial Differetial Equations*, vol. 21, pp. 770–790.

Melenk, J. M.; Babuška, I. (1996): The partition of unity finite element method: Basic theory and applications. *Computer Methods in Applied Mechanics and Engineering*, vol. 139, pp. 289–314.

Tada, H.; Paris, P. C.; Irwin, G. R. (2000): *Analysis of crack handbook*. The American Society of Mechanical Engineers, New York, USA, third edition.

Timoshenko, S.; Goodier, J. (1970): *Theory of elasticity*. McGraw-Hill, New York, USA, 3rd edition.

Wang, J. G.; Liu, G. R. (2002): A point interpolation meshless method based on radial basis functions. *International Journal for Numerical Methods in Engineering*, vol. 54, pp. 1623–1648.

Wanger, G. J.; Liu, W. K. (1999): Applied of essential boundary conditions in meshfree methods: a corrected collocation method. *International Journal for Numerical Methods in Engineering*, vol. 47, pp. 1367–1379.

Zhang, Y.; Chen, L. (2008): A simplified meshless method for dynamic crack growth. *CMES: Computer Modeling in Engineering & Sciences*, vol. 31, no. 3, pp. 189–200.

Zheng, C.; Wu, S. C.; Tang, X. H.; Zhang, J. H. (2008): A meshfree poly-cell Galerkin (MPG) approach for problems of elasticity and fracture. *CMES: Computer Modeling in Engineering & Sciences*, vol. 38, no. 2, pp. 149–178.

Zhu, T.; Atluri, S. (1998): A modified collocation method and a penalty formulation for enforcing the essential condition in the element free Garlerkin method. *Computational Mechanics*, vol. 21, no. 3, pp. 211–222.

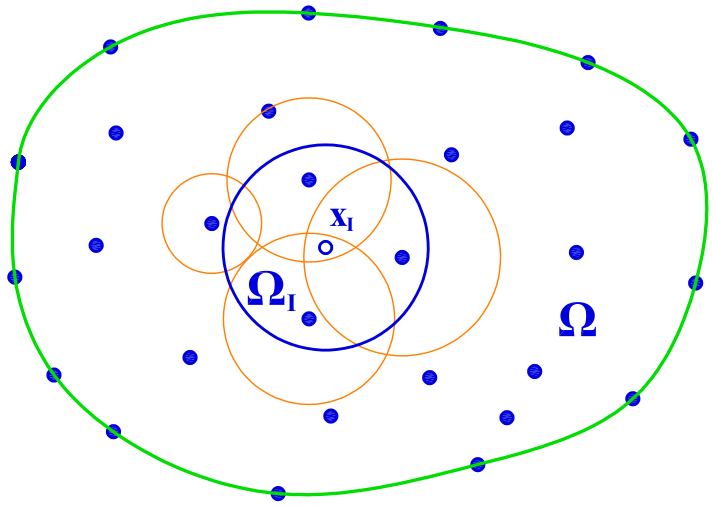

Figure 1: Schematic representation of a Moving IRBFN: Ω is the domain of interest which is subdivided into N overlapping subdomains Ω_I centered at $\mathbf{x}_I$.

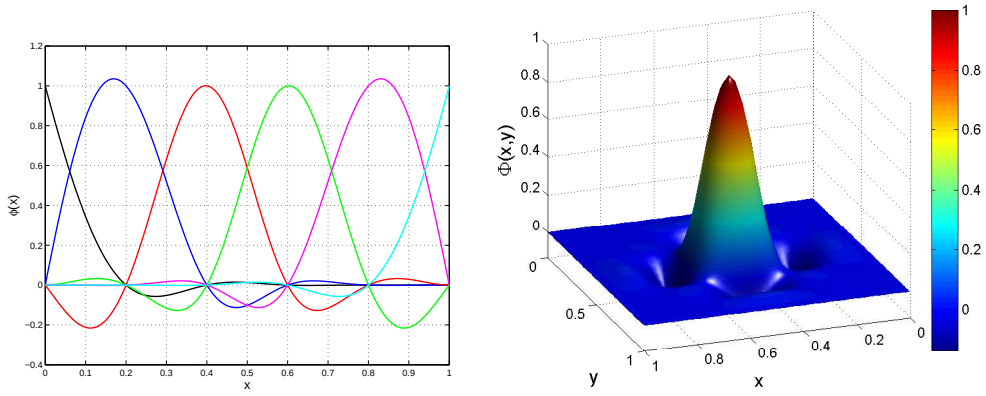

(a) (b)

Figure 2: Example of Moving IRBFN shape functions: (a) $\Phi_I(x)$ in one dimension and (b) $\Phi_I(x,y)$ in two dimensions.

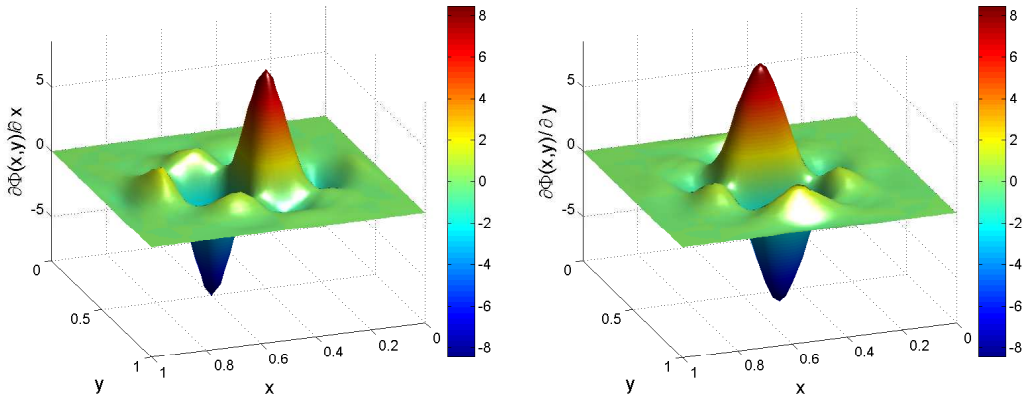

Figure 3: Example of derivatives of Moving IRBFN shape functions in two dimensions: (a) $\frac{\partial \Phi_I}{\partial x}(x,y)$ and (b) $\frac{\partial \Phi_I}{\partial y}(x,y)$.

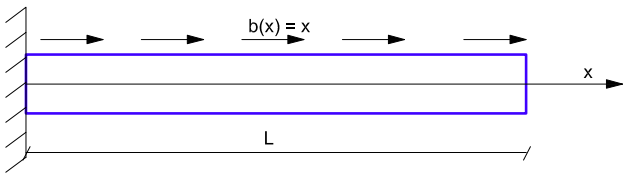

Figure 4: A uniform bar: a mathematical model.

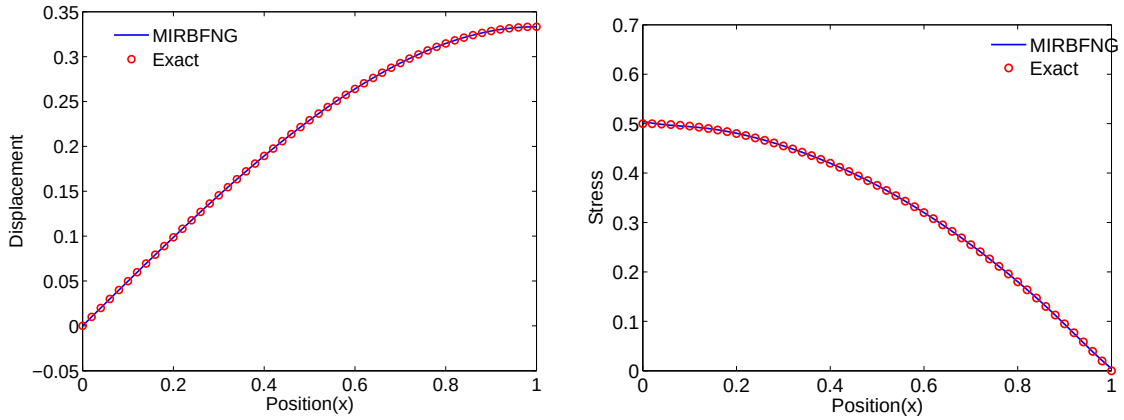

(a) (b)

Figure 5: A uniform bar: the results obtained by the present method with 9 nodes are interpolated at 50 nodes, (a) displacement and (b) stress.

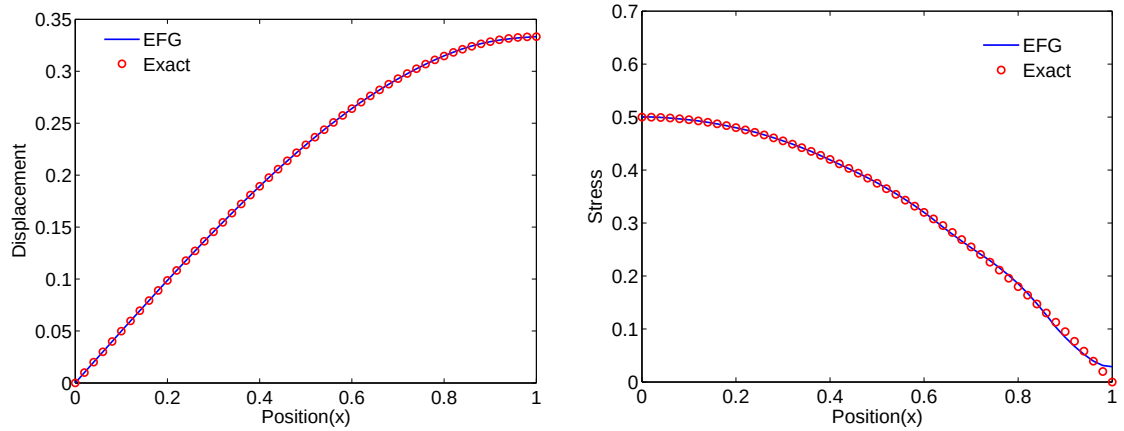

(a) (b)

Figure 6: A uniform bar: the results obtained by the EFG method with 9 nodes are interpolated with 50 nodes, (a) displacement and (b) stress.

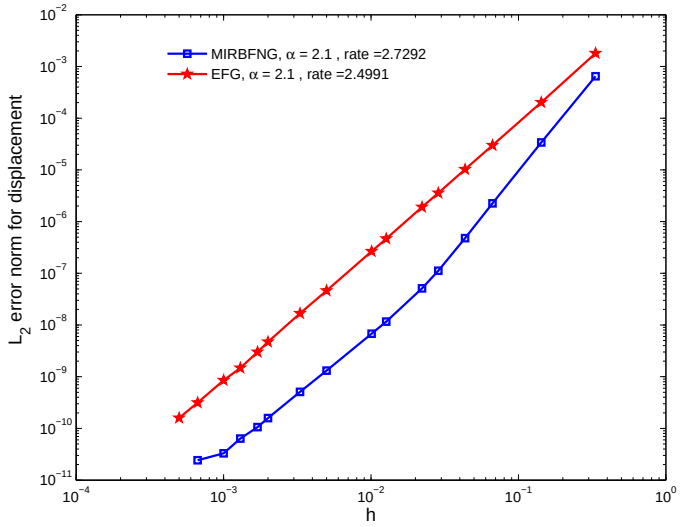

Figure 7: A uniform bar: L_2 error norm for displacement.

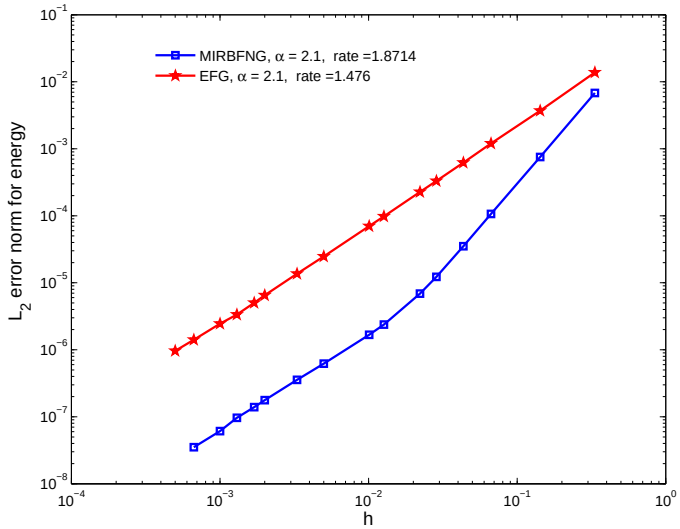

Figure 8: A uniform bar: L_2 error norm for energy.

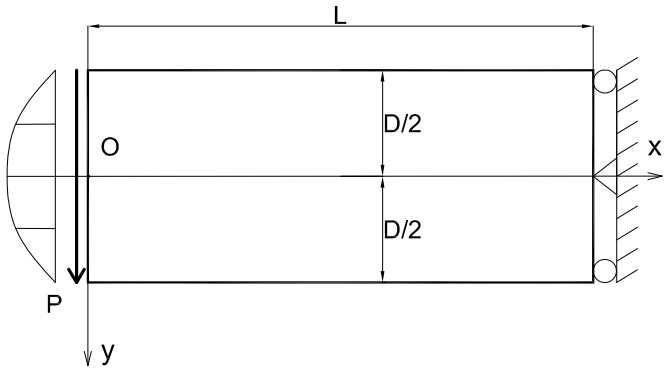

Figure 9: Cantilever beam: a mathematical model.

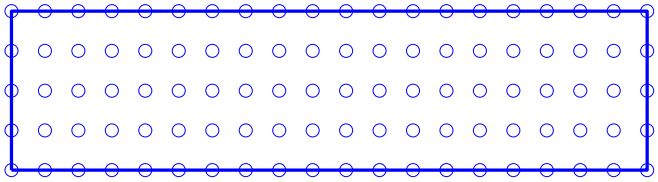

Figure 10: Cantilever beam: discretisation model with 20×5 nodes.

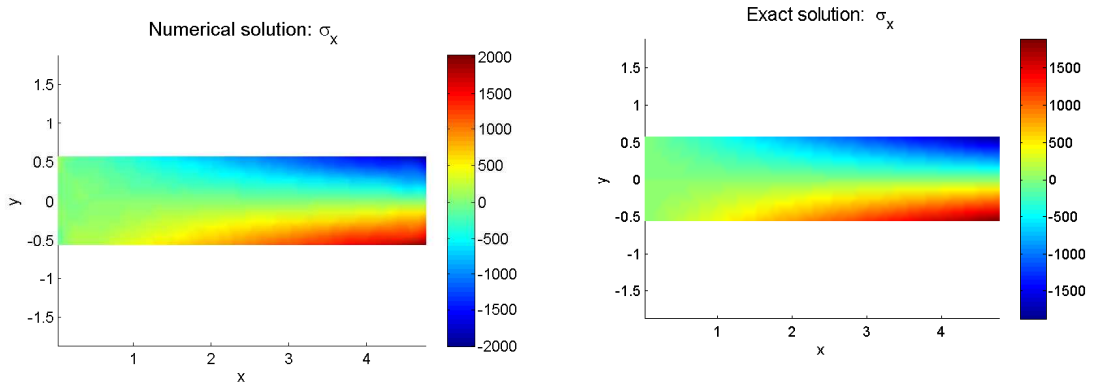

(a) (b)

Figure 11: Cantilever beam: σ_x given by (a) MIRBFNG with 20×5 nodes and (b) Exact solution.

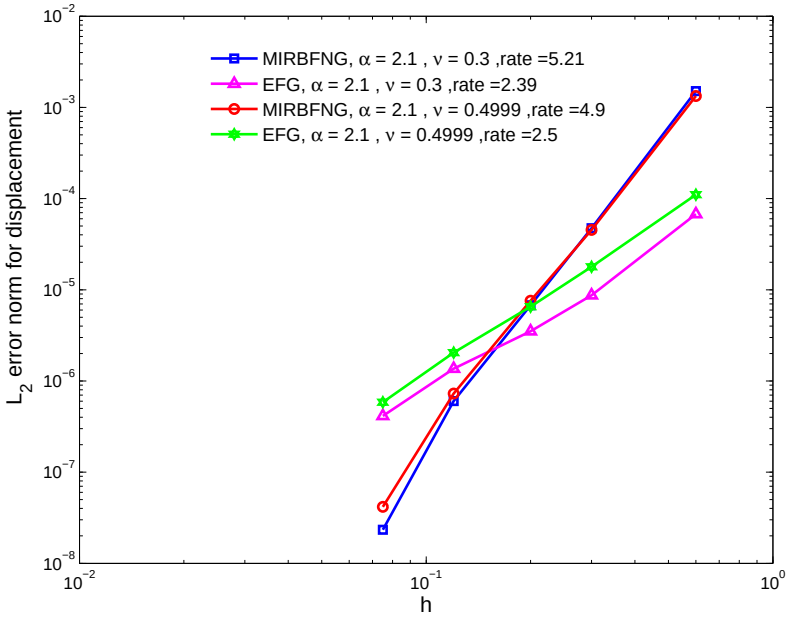

Figure 12: Cantilever beam: L_2 error norm for displacement.

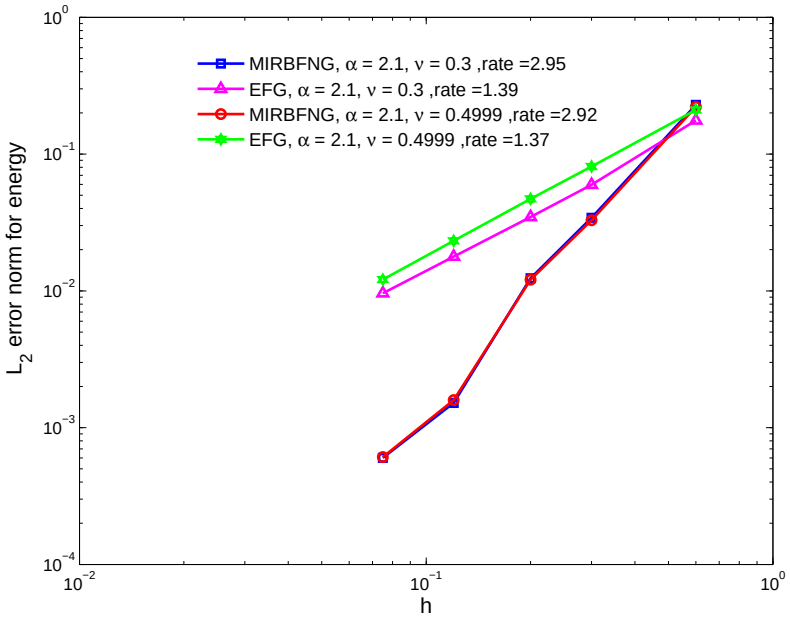

Figure 13: Cantilever beam: L_2 error norm for energy.

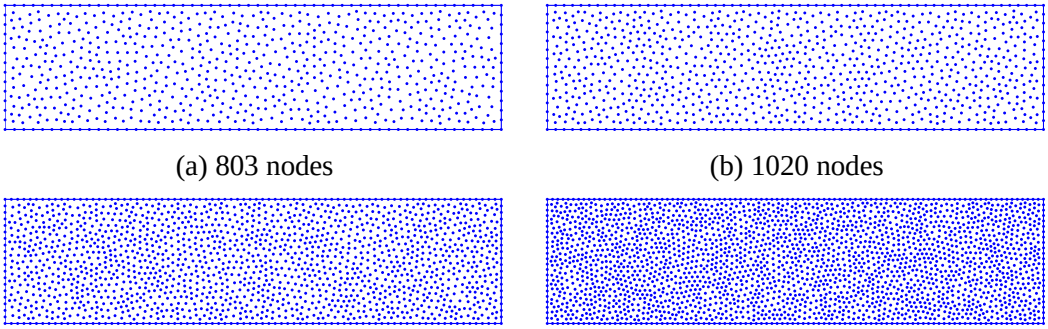

(a) 803 nodes (b) 1020 nodes

(c) 1725 nodes (d) 2502 nodes

Figure 14: Cantilever beam: untructured discretisations.

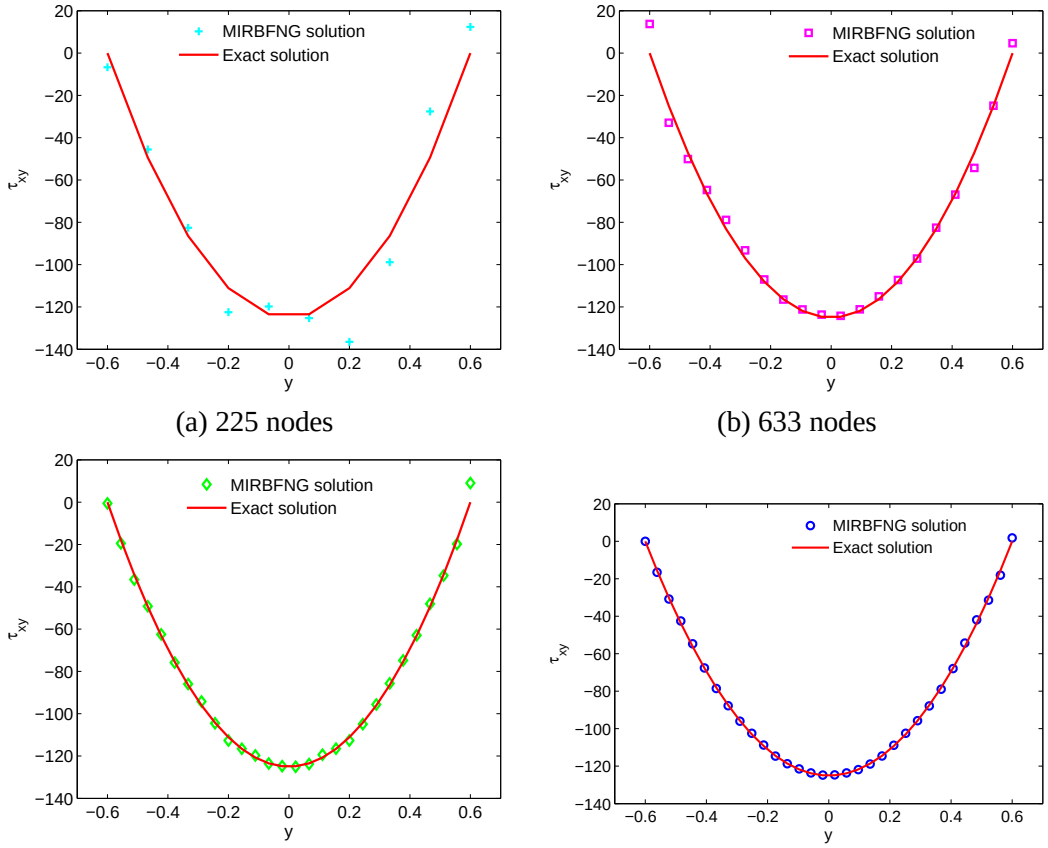

(a) 225 nodes (b) 633 nodes

(c) 803 nodes (d) 1020 nodes

Figure 15: Cantilever beam: convergence of τ_{xy} at $x = 2.40$ with untructured nodal refinement.

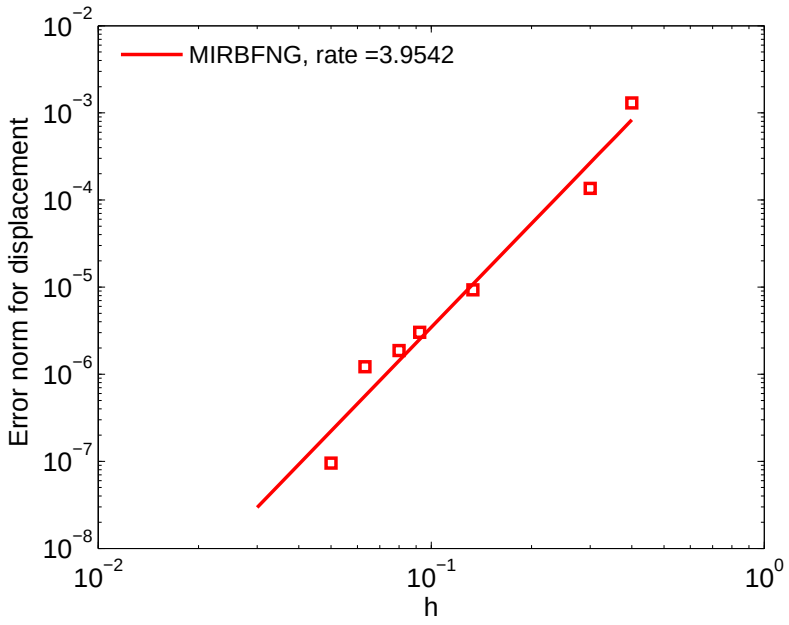

Figure 16: Cantilever beam: L_2 error norm for displacement with unstructured nodes.

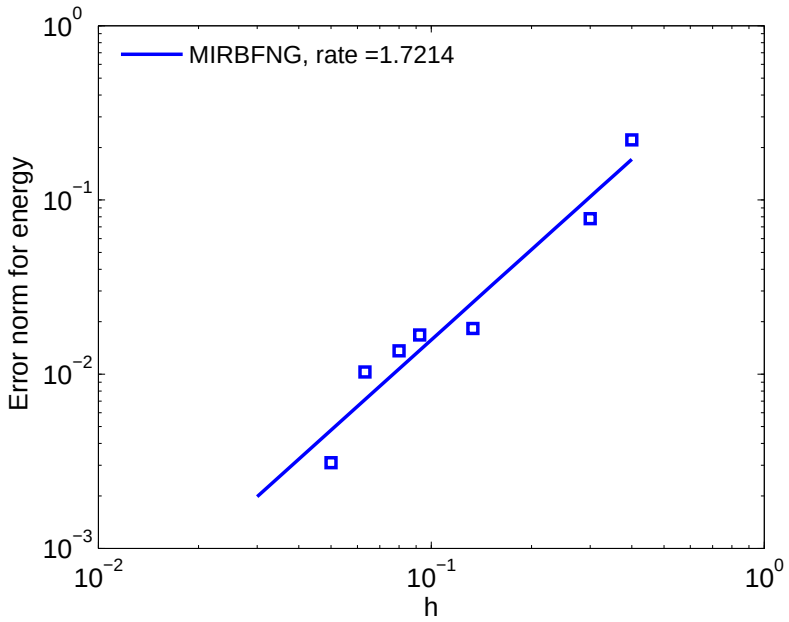

Figure 17: Cantilever beam: L_2 error norm for energy with unstructured nodes.

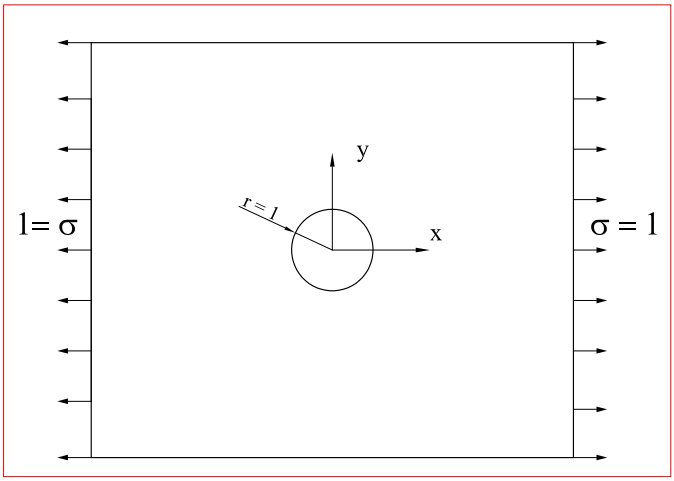

Figure 18: Infinite plate with a circular hole.

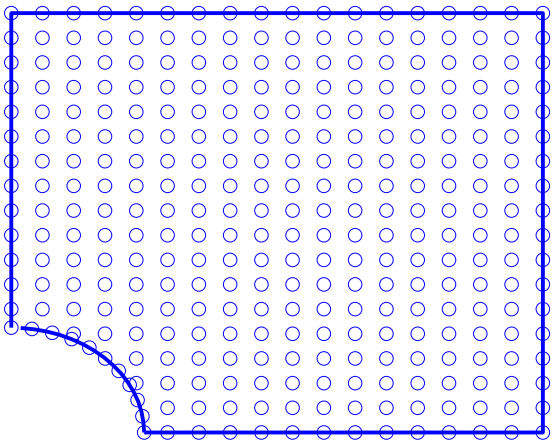

Figure 19: Infinite plate with a circular hole: computational domain discretization with 315 nodes.

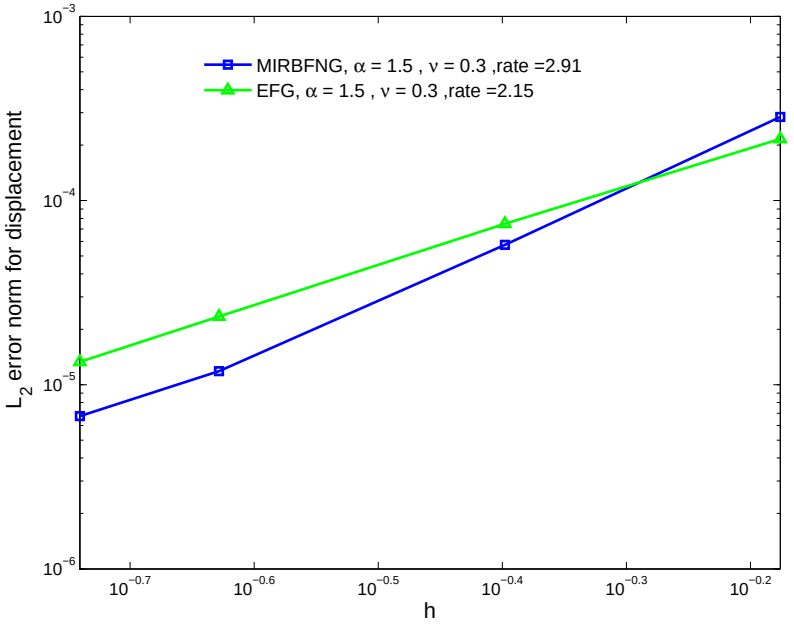

Figure 20: Infinite plate with a circular hole: L_2 error norm for displacement.

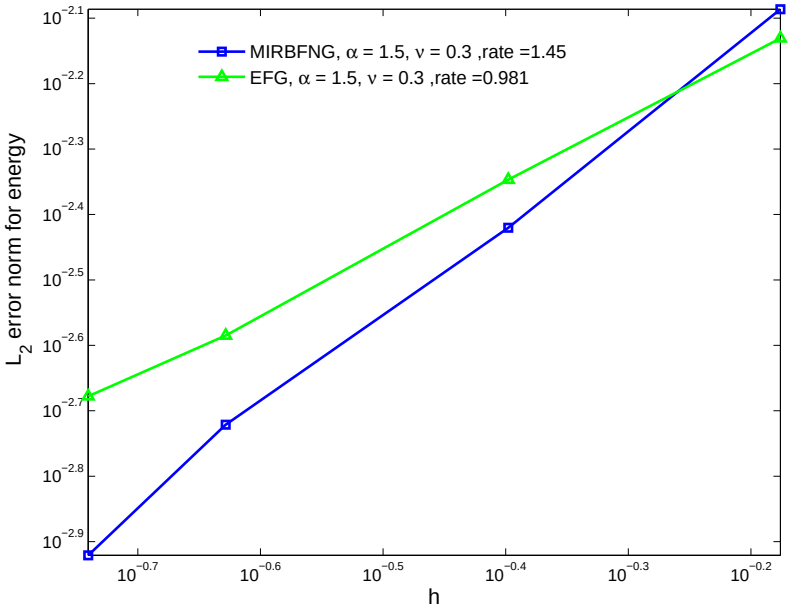

Figure 21: Infinite plate with a circular hole: L_2 error norm for energy.

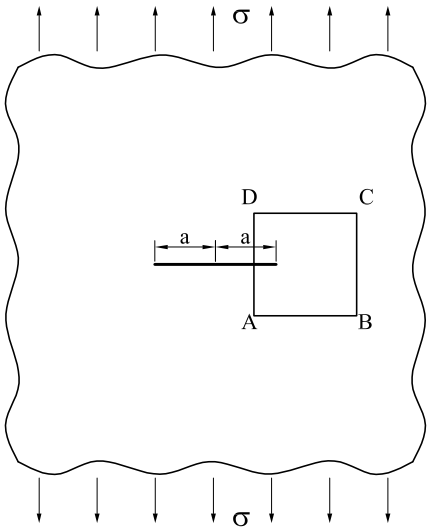

Figure 22: Infinite cracked plate under remote tension.

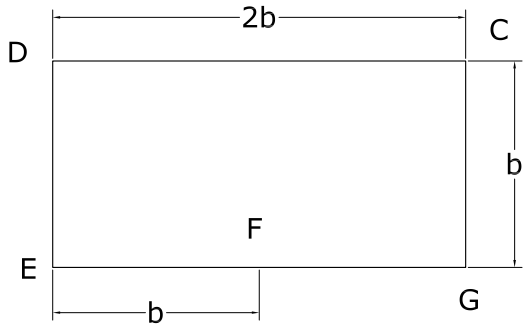

Figure 23: Infinite cracked plate: analyzed portion.

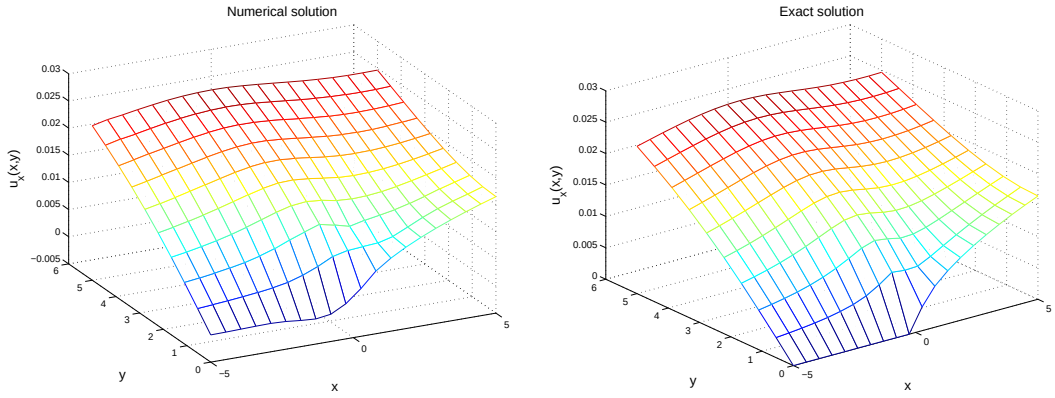

(a) (b)

Figure 24: Infinite cracked plate: (a) MIRBFNG solution and (b) exact solution of u_x with 20×10 nodes ($\mu = 0.3$).

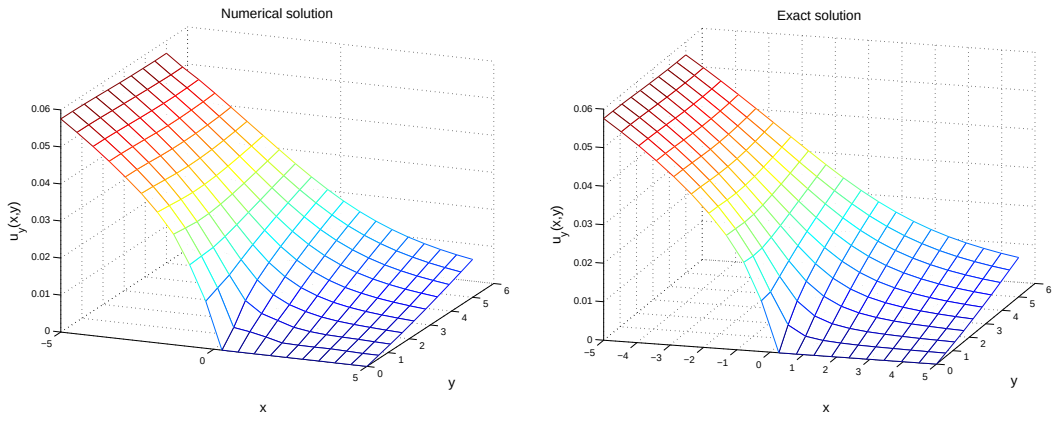

(a) (b)

Figure 25: Infinite cracked plate: (a) MIRBFNG solution and (b) exact solution of u_y with 20×10 nodes ($\mu = 0.3$).

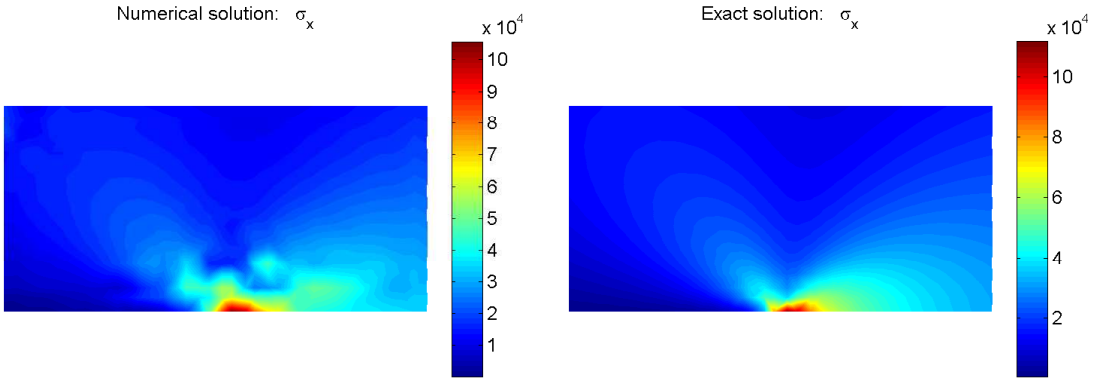

(a) (b)

Figure 26: Infinite cracked plate: (a) MIRBFNG solution and (b) exact solution of σ_x with 20×10 nodes ($\mu = 0.3$).

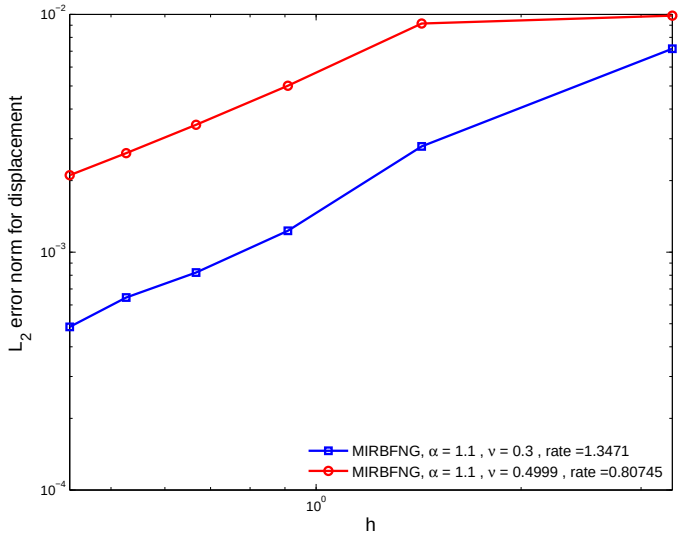

Figure 27: Infinite cracked plate: L_2 error norm for displacement.

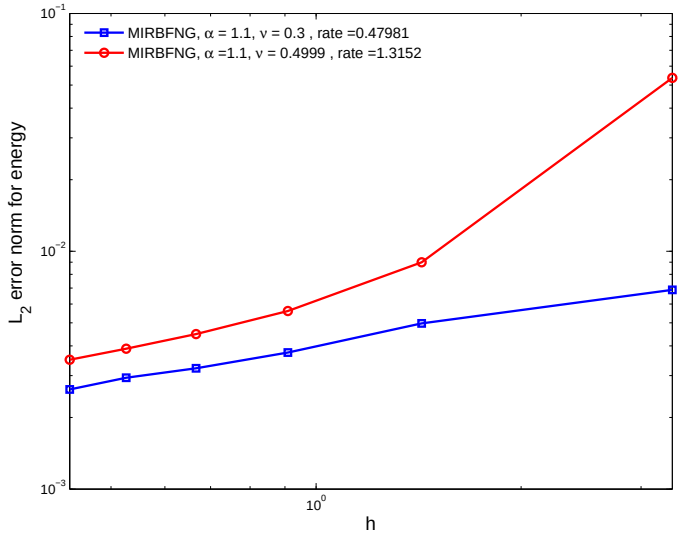

Figure 28: Infinite cracked plate: L_2 error norm for energy.